

Impact of Dust on climate and AMOC during the Last Glacial Maximum Simulated by CESM1.2

Ming Zhang¹, Yonggang Liu¹, Jiang Zhu², Zhuoqun Wang¹, and Zhengyu Liu³

¹Peking University

²National Center for Atmospheric Research

³Ohio State University

November 24, 2022

Abstract

While the impact of dust on climate and Atlantic Meridional Overturning Circulation (AMOC) during the interglacial period such as the mid-Holocene (MH) has been studied extensively, its impact during the glacial period is unclear. Here we investigate how the climate and AMOC would change if there had been no dust during the Last Glacial Maximum (LGM). Model simulations show that the dust removal leads to a global cooling of over 2.4 °C and a weakening of AMOC by ~30 %. Such temperature change is opposite in sign to that for the MH. The cooling is attributed to the increase of snow and ice albedo and weakening of AMOC when dust is removed, and is amplified through a positive feedback between sea ice and AMOC. Our results indicate that the climate and AMOC are more sensitive to dust change during the glacial than the interglacial period.

25 **Abstract**

26 While the impact of dust on climate and Atlantic Meridional Overturning Circulation (AMOC)
27 during the interglacial period such as the mid-Holocene (MH) has been studied extensively, its
28 impact during the glacial period is unclear. Here we investigate how the climate and AMOC
29 would change if there had been no dust during the Last Glacial Maximum (LGM). Model
30 simulations show that the dust removal leads to a global cooling of over 2.4 °C and a weakening
31 of AMOC by ~30 %. Such temperature change is opposite in sign to that for the MH. The
32 cooling is attributed to the increase of snow and ice albedo and weakening of AMOC when dust
33 is removed, and is amplified through a positive feedback between sea ice and AMOC. Our
34 results indicate that the climate and AMOC are more sensitive to dust change during the glacial
35 than the interglacial period.

36

37

38

39

40

41

42

43

44

45

46

47

48 **Plain language summary**

49 Dust in the atmosphere reflects and absorbs sunlight, reducing the shortwave radiation reaching
50 the surface, while the dust deposited on snow and ice reduces the surface albedo and increases
51 the shortwave radiation received at the surface. Our previous work (Zhang et al. 2021) showed
52 dust reduction during the interglacial period (e.g. mid-Holocene; MH) would cause a global
53 warming of 0.1 °C and a weakening of AMOC by 6.2 %. This warming was due to more sunlight
54 received at the surface when atmospheric dust is removed. Here we show that if dust was
55 removed during the Last Glacial Maximum, climate will be cooled significantly rather than
56 warmed. The major reason is that snow on land was much more extensive during LGM than MH,
57 such that the increase of snow albedo after dust removal has a dominating effect on climate.
58 Result suggests that the global climate and AMOC in the glacial period are more sensitive to dust
59 change than those in the interglacial period.

60

61

62

63

64

65

66

67

68

69

70

71 **1. Introduction**

72 Dust in the atmosphere reduces the solar insolation received at the surface by reflecting and
73 absorbing sunlight, while dust falling on snow and ice increases the solar insolation received at
74 the surface by reducing the surface albedo. Therefore, variations of surface dust flux and
75 atmospheric dust concentration can affect local and maybe even global climate. On orbital
76 timescales, both dust flux and atmospheric dust concentration fluctuate (Kohfeld and Harrison
77 2001; Lambert et al. 2008). For example, during the mid-Holocene (MH; 6 ka), dust emission
78 from both North Africa and Arabian Peninsula was much lower than present day (deMenocal et
79 al. 2000; Mashayek and Peltier 2013; McGee et al. 2013; Pausata et al. 2016; Zheng et al. 2013).
80 Such reduction has been shown to affect African monsoon (Pausata et al. 2016; Thompson et al.
81 2019), tropical cyclone frequency and intensity (Pausata et al. 2017a), El Niño – Southern
82 Oscillation (ENSO; Pausata et al. 2017b), East Asian climate (Huo et al. 2021; Sun et al. 2019)
83 and Atlantic Meridional Overturning Circulation (AMOC; Zhang et al. 2021). Globally, the dust
84 reduction might have induced a global warming of the order 0.1 °C (Liu et al. 2018; Zhang et al.
85 2021). During the glacial periods, the global dust fluxes are two to five times greater than present
86 day (Kohfeld and Harrison 2001; Maher et al. 2010). However, the role of dust in the global
87 climate and ocean circulation during such periods is still unclear.

88

89 The Last Glacial Maximum (LGM; 21 ka) is the nearest glacial period to us, during which the
90 greenhouse gas concentrations (GHGs), glaciers, orbital configuration and thus the climate were
91 different from the present (Braconnot et al. 2007; Kageyama et al. 2017). Proxy reconstructions
92 indicate that the global mean surface temperature (GMST; all temperatures herein are annual
93 mean) during the LGM was 4.4-6.8 °C lower than that in the pre-industrial (PI; Tierney et al.

94 2020). The deep-ocean stratification was strengthened during the LGM, mainly due to the
95 increase of abyssal salinity (Adkins et al. 2002). Accordingly, the North Atlantic Deep Water
96 (NADW) was shallower and the Antarctic Bottom Water (AABW) expanded compared to
97 present-day counterparts (Bohm et al. 2015; Curry and Oppo 2005; Lynch-Stieglitz et al. 2007;
98 Marchitto and Broecker 2006).

99

100 The increase of dust emission during the LGM was mainly due to the increase in wind speeds,
101 weakening of the hydrological cycle and expansion in dust source areas (Harrison et al. 2001).
102 Both the observed and simulated results show that atmospheric dust loading during the LGM was
103 2-3 times of that in present day (Kohfeld and Harrison 2001; Maher et al. 2010; Mahowald et al.
104 2006b; Werner et al. 2002). The dust deposition rate in polar region even increased by ~20 times
105 (Hansson 1994; Lambert et al. 2008; Mayewski et al. 1994; Petit et al. 1990; Steffensen 1997;
106 Steffensen et al. 2008).

107

108 Many studies have investigated the emission and atmospheric loading of dust as well as its
109 influence on radiation, surface temperature and African monsoon etc. during the LGM (Albani
110 and Mahowald 2019; Albani et al. 2014; Mahowald et al. 2006a; Mahowald et al. 2006b;
111 Ohgaito et al. 2018; Sagoo and Storelvmo 2017; Shen et al. 2020). For example, Albani et al.
112 (2014) optimized the dust emission, particle size and optical properties in CAM4 and obtained a
113 dust distribution that best fits reconstructions. They also emphasized the importance of dust's
114 optical properties and size distribution on the estimation of direct radiative effect and the
115 influence on monsoon (Albani and Mahowald 2019). Dust deposition on snow was able to cause
116 a significant warming (3-5 °C) over Tibet Plateau surface through snow-darkening effect (i.e.

117 reducing surface albedo by darkening snow and increasing snowmelt; Hansen and Nazarenko
118 2004; Qian et al. 2014; Shi et al. 2019) during LGM (Shen et al. 2020), showing a much larger
119 influence than in mid-Holocene (Zhang et al. 2021). In the latest Paleoclimate Model
120 Intercomparison Project phase 4 (PMIP4), changes and uncertainties of the dust are also
121 considered in the sensitivity experiments for LGM (Kageyama et al. 2017). However, there has
122 been no attempt to answer the question as to what the climate would have been if there had been
123 no dust during the LGM.

124

125 Here we aim to answer this question by modeling the LGM climate both with and without dust.
126 As will be shown later, the impact of dust on LGM climate is much larger than that on the MH
127 climate, and the sign of impact on the GMST is the opposite. We also pay special attention to the
128 impact on AMOC which plays an important role in controlling glacial-interglacial climate shifts
129 by regulating the meridional heat transport and the carbon storage in deep ocean (Brovkin et al.
130 2007; Denton et al. 2010; Smith and Gent 2010).

131

132 **2. Model and experiments**

133 **2.1 Model description**

134 The fully coupled climate model used here is the Community Earth System Model version 1.2.2
135 (CESM1.2.2) (<http://www2.cesm.ucar.edu/>), which reproduces the observed climate features
136 reasonably well among the Coupled Model Intercomparison Project phase 5 (CMIP5) models
137 (Knutti et al. 2013). The atmosphere model, Community Atmosphere Model version 5 (CAM5),
138 represents the aerosol size distribution with a 3-mode Modal Aerosol Model parameterization
139 (CAM5-MAM3) (Neale et al. 2010). The emission, transport and wet and dry deposition of dust

140 are all treated in the dust module (Ganopolski et al. 2010). In CAM5, only the direct radiative
141 effect of dust is considered (Albani et al. 2014; Neale et al. 2010). The Community Land Model
142 version 4 (CLM4; Lawrence et al. 2011) involves an active carbon-nitrogen (CN)
143 biogeochemical cycle. The snow-darkening effect of dust is considered based on the Snow, Ice
144 and Aerosol Radiation model (SNICAR) (Flanner and Zender 2006; Flanner et al. 2009). The
145 ocean model, Parallel Ocean Program version 2 (POP2; Smith and Gent 2010) uses a new
146 overflow parameterization (OFP; Briegleb et al. 2010) to represent the Nordic Sea overflows
147 (Denmark strait and Faroe Bank Channel) and the Antarctic overflows (Ross Sea and Weddell
148 Sea), which improved the simulations of Gulf Stream path and AMOC (Danabasoglu et al.
149 2012).

150

151 In this study, a horizontal resolution of latitude $1.9^\circ \times$ longitude 2.5° is used for both the
152 atmosphere and land. Both the ocean and sea ice adopt the nominal 1° resolution, which has
153 uniform 1.125° spacing in latitude and uneven spacing in longitude (0.27° near the equator,
154 gradually increasing to the maximum 0.65° at 60° N/S and then decreasing poleward). The north
155 pole of the ocean and sea-ice grids resides in Greenland. In the vertical direction, the atmosphere
156 and ocean grids have 30 and 60 layers, respectively.

157

158 **2.2 Experiment setup**

159 A summary of the experimental setup is provided in Table S1. One LGM control experiment
160 (called LGMctl) with an active dust cycle and one sensitivity experiment removing dust (called
161 LGMND) are carried out. The orbital forcing and GHGs in both experiments follow the
162 Paleoclimate Modelling Intercomparison Project phase 3 (PMIP3) protocol. Land ice sheets

163 (LISs) and the associated changes of sea level and land-sea mask are derived from reconstructed
164 ice-6G model (Peltier et al. 2015). The PI vegetation cover is prescribed in both experiments but
165 the vegetation phenology responds to climate change according to an active CN biogeochemical
166 cycle (Lawrence et al. 2011). In LGMctl, distribution of surface dust sources is the same as that
167 in PI, neglecting their changes due to glacial dynamics, sea level drop and vegetation changes
168 (Albani et al. 2014; Harrison et al. 2001; Mahowald et al. 2006b). In LGMND, dust is removed
169 by setting the soil erodibility to zero everywhere.

170
171 The LGMctl experiment was integrated for 4000 years. The GMST and the AMOC strength
172 (defined as the maximum Atlantic meridional streamfunction below 500 m depth) still drift at
173 rates of 0.056 °C/1000 year and -0.18 Sv/1000 years, respectively, for the final 1000 years. The
174 LGMND experiment was branched from the year 4001 of LGMctl and run for 1200 years. The
175 drifts of GMST and AMOC strength are -0.15 °C/1000 years and -2.16 Sv/1000 years,
176 respectively (diagnosed using the final 500 years, Figure S1). As will be seen later, such small
177 drift neither prevents us from understanding the results and mechanism of dust impact nor affects
178 the major conclusions. The final 200 years of data of both experiments are used for analysis.

179
180 In order to understand the mechanisms of climate change more clearly, a pair of atmosphere-only
181 experiments, one with dust (LGM_fixedSST) and the other without dust (LGMND_fixedSST),
182 were also carried out in which the sea surface temperature (SST) and sea-ice concentration from
183 LGMctl are prescribed. The direct impact of dust on climate (i.e. without the feedbacks of ocean
184 and sea ice) can be demonstrated by the results of such experiments. A pair of experiments with
185 slab ocean (LGM_SOM and LGMND_SOM) were also performed to include the feedback from

186 sea-ice thermodynamics but not the effect of ocean dynamics. To test the influence of the
187 uncertainty in dust emission, we also carried out a pair of prescribed-SST experiments with a
188 different dust source distribution (LGM_fixedSST_gladst and LGMND_fixedSST). More details can
189 be found in Text S1.

190

191 **3. LGM climatology**

192 The simulated GMST by LGMctl is 7.66 °C (Table S1), 7.39 °C lower than that in PI (15.05 °C)
193 simulated by the same model with the same resolution. A global surface cooling of 6.8 °C during
194 LGM with CESM1.2.2 was obtained in Zhu and Poulsen (2021) following the PMIP4 protocol
195 (Kageyama et al. 2017), which is within the estimated range of reconstructions (95 % confidence
196 interval: -6.8 ~ -4.4 °C; Tierney et al. 2020). The lower LGM temperature here is probably due to
197 two reasons: 1) the vegetation phenology is simulated online, resulting in an increase in surface
198 albedo (Lawrence et al. 2011); 2) the CO₂ concentration used here is slightly lower than that
199 suggested by the PMIP4 protocol (Kageyama et al. 2017). The LGM GMST obtained here is not
200 much colder than the proxy estimates. Compared to PI, cooling occurs all over the world,
201 especially over the elevated continental glaciers and polar oceans where sea ice expands (Figure
202 S2a). Consistent with the surface cooling, the annual-mean precipitation in LGM decreases in
203 most parts of the world, with a global average reduction of 0.49 mm/day (Figure S2b).

204

205 The major characteristics of ocean stratification and MOC in LGMctl agree well with the
206 reconstructions (Adkins et al. 2002; Adkins et al. 2005; Curry and Oppo 2005; Marchitto and
207 Broecker 2006), including saltier and colder water in the deep Southern Ocean (Figures S3a-b),
208 strengthened ocean stratification dominated by salinity change (Figure S3c), a shallower NADW

209 (Figures S3d-f) and an expanded AABW (Figures S3g-i).

210

211 Both total dust emission and atmospheric dust loading simulated by LGMctl are approximately

212 twice those in PI (6369.17 Tg/year vs 3103.57 Tg/year for dust emission; 41.96 Tg vs 21.83 Tg

213 for dust loading) (Table S1), mainly attributed to the increased wind speeds and weakened

214 hydrological cycle. Distribution of dust emission sources and atmospheric dust loading in

215 LGMctl are similar to those in PI (Figure S4). The ratio of global dust loading between LGM

216 and PI in our work is within the range from previous studies (Albani and Mahowald 2019; Maher

217 et al. 2010; Takemura et al. 2009; Werner et al. 2002). The possible influence of glaciogenic dust

218 source suggested by Mahowald et al. (2006b) and Albani et al. (2014) is briefly discussed in

219 section 6.

220

221 **4. Climate and AMOC responses to dust removal**

222 After the dust removal, the simulated LGM GMST decreases by 2.42 °C (Table S1), indicating

223 that dust had a significant warming effect during the LGM. This is opposite to the effect of dust

224 during MH, where dust removal led to a weak global warming (Zhang et al. 2021). The cooling

225 induced by dust removal during the LGM occurs almost everywhere, with the most significant

226 cooling in the high latitudes of both hemispheres (up to 20 °C; Figure 1a) where sea ice expands

227 and thickens (Figure 1g). There is an obvious cooling (~4 °C) over the dust source areas, such as

228 North Africa, Arabian Peninsula, and Central and Western China. Cooling is also seen over the

229 Tibet Plateau, North America and Europe, most likely due to increase in snow depth after the

230 dust removal (Figure 1h, see section 5.2 for more details). Albani and Mahowald (2019) showed

231 that the presence of dust during LGM induced a global warming of 0.15 °C, much weaker than

232 obtained here. This may be because 1) their simulations were run for only 50 years; 2) the
233 atmospheric module of their model was CAM4, while CAM5 is used herein, both the LGM
234 climatology and its response to dust could be different between the two models. Specifically, the
235 LGM GMST simulated by CAM5 is 2.44 °C lower than that in CAM4 (Kageyama et al. 2021),
236 which may amplify the responses of snow and sea ice in high latitudes after dust removal here.

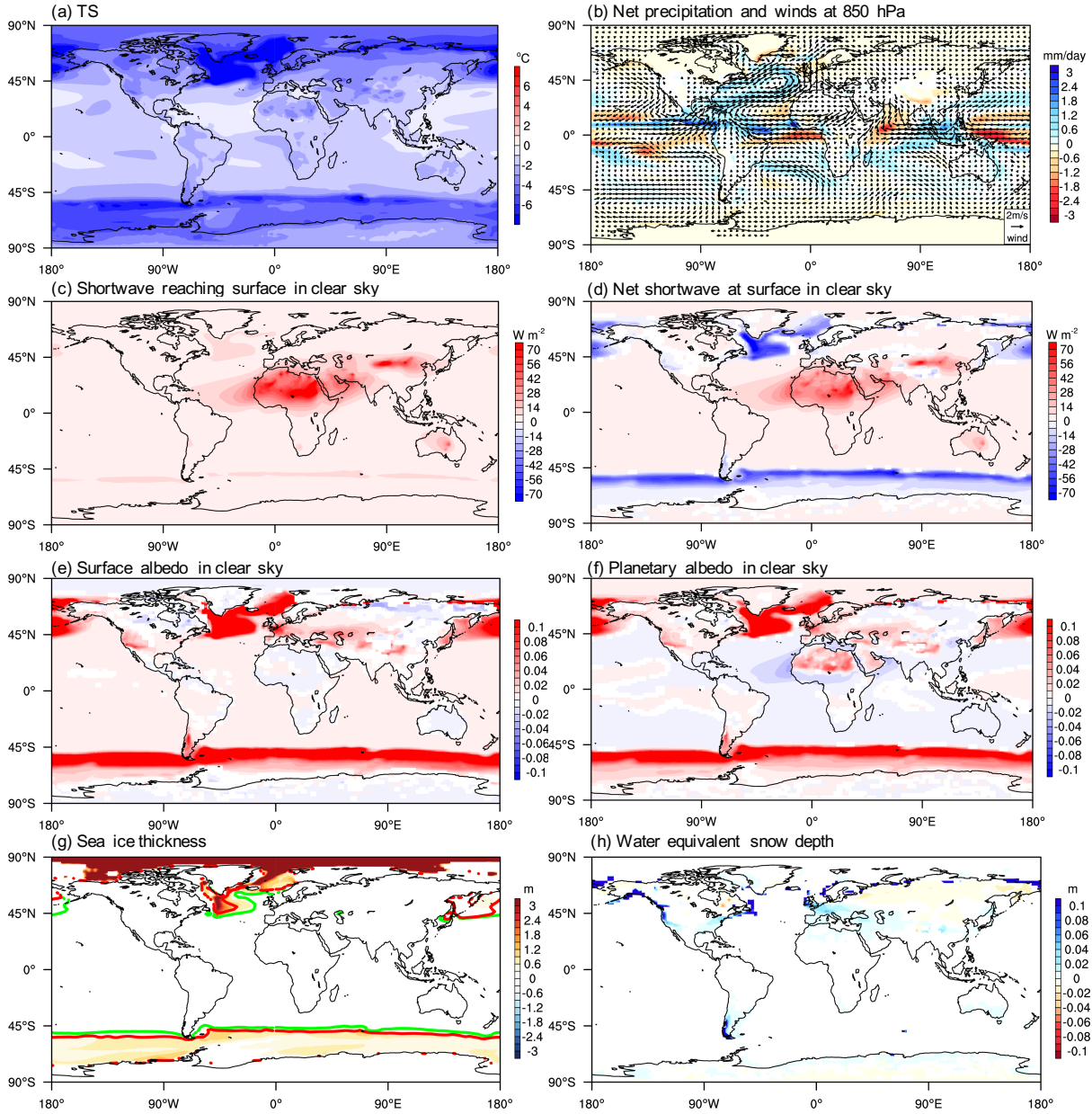
237

238 The annually averaged global-mean precipitation decreases by 0.05 mm/day after dust removal
239 (Table S1). The net precipitation over North Africa is reduced due to the weakened West African
240 summer monsoon; at the same time, anomalous easterly winds bring water vapor to the western
241 North Atlantic, causing an increase in net precipitation there (Figure 1b). This pattern of change
242 in net precipitation is similar to that in MH. The net precipitation also increases over the northern
243 North Atlantic (north of 45° N), but it is mainly due to the decreased local evaporation (not
244 shown).

245

246 The AMOC weakens continuously for 700 years after dust is removed (Figure S1b), and
247 becomes 7.71 Sv (-28.7 %) weaker than before dust is removed at the end of simulation (Table
248 S1). Not only weaker, the AMOC is also slightly shallower than before dust is removed (Figure
249 2a). The maximum March mixed layer depth over Irminger Sea becomes significantly shallower
250 (up to 700 m, Figure 2b), in line with the weakened AMOC. The global northward oceanic heat
251 transport (OHT) across 50° N is reduced by 0.32 petawatt (Figure 2c), also consistent with the
252 weakening of AMOC. The response of AMOC to dust removal is in the same direction as that in
253 MH but has a much larger magnitude, indicating a dependence on background climate state.

254

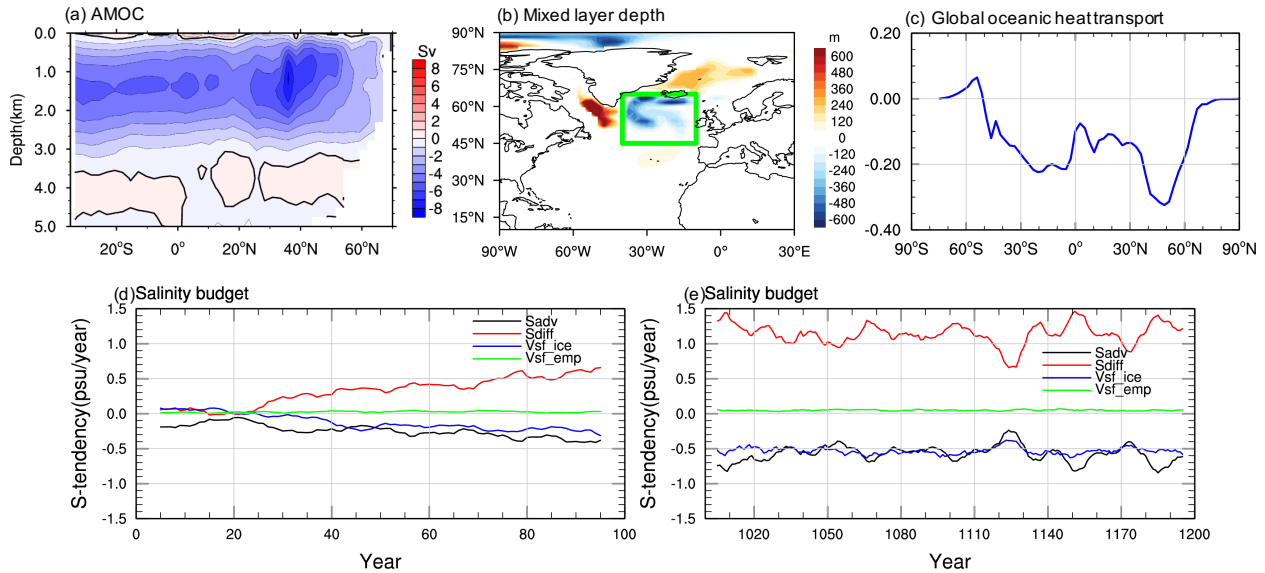


255

256 **Figure 1.** Anomalies of annual mean (a) surface temperature (unit: °C), (b) net precipitation (unit:
 257 mm/day) and 850 hPa winds (unit: m/s), (c) downward shortwave radiation at the surface under
 258 clear-sky condition (unit: $W m^{-2}$), (d) net shortwave radiation at the surface under clear-sky
 259 condition (unit: $W m^{-2}$), (e) clear-sky surface albedo, (f) clear-sky planetary albedo, (g) sea-ice
 260 thickness (unit: m) and (h) water equivalent snow depth (unit: m) in the LGMND experiment
 261 compared to LGMctl. The green contours and red contours in (g) are the sea-ice margin (defined

262 as 15 % grid-cell sea-ice coverage) in LGMND and LGMctl, respectively. Only regions
 263 with >90 % confidence level (calculated by two-tailed student-t test) are shown.

264



265

266 **Figure 2.** Changes of annual mean Atlantic meridional streamfunction (AMSF, unit: Sv),
 267 maximum March mixed layer depth (unit: m) in the Atlantic and global oceanic heat transport
 268 (unit: Pw) when dust is removed are shown in a-c and the evolution of anomalies of the terms in
 269 the salinity budget equation (Zhang et al. 2021) after dust removal are shown in d-e (unit:
 270 psu/year). Zero contour lines are shown in black in (a). The green box (45° N-65° N, 40° W-10°
 271 W) in (b) indicates the region where salinity budget is calculated. (d) is for anomalies of the first
 272 100 years and (e) is for anomalies of last 200 years. A moving average of 10 years has been
 273 applied to all curves in d-e. The black curve is for horizontal advection (Sadv); red is for
 274 diffusion (horizontal plus vertical; Sdiff); blue is for virtual salt flux (VSF) due to sea-ice
 275 melting/formation (Vsf_ice); green is for VSF due to net evaporation (Vsf_emp, evaporation
 276 minus precipitation minus runoff).

277

278 **5. Mechanism analyses**

279 **5.1 Global surface cooling**

280 The annual-mean shortwave radiation reaching the surface increases (Figure 1c) after dust is
281 removed, especially over regions where atmospheric dust loading was high (Figure S4b). The
282 increased radiation over tropical North Atlantic warms the ocean surface there (Figures 1a, S5a
283 and S5d). However, the net shortwave radiation received by the surface is reduced (Figure 1d)
284 over high latitudes of both hemispheres due to sea ice expansion and thickening (Figure 1g) and
285 over various plateaus (e.g. the Rockies, Iranian and Tibetan Plateau) due to increased snow depth
286 (Figure 1h), all leading to higher surface albedo (Figure 1e). The increase in snow depth is
287 because of the disappearance of snow-darkening effect when there is no dust, while the
288 expansion of sea ice will be analyzed further below. Before that, note that the clear-sky planetary
289 albedo increases over the Sahara and the Arabian region (Figure 1f), where the atmospheric dust
290 loading was the heaviest before being removed (Figure S4b). This means that although this
291 region receives more net shortwave radiation at the surface (Figure 1d), the surface plus the
292 whole atmospheric column actually receives less energy from the Sun when dust is removed.
293 This change of planetary albedo over North Africa and Arabian region is similar to that in Albani
294 et al. (2014) and Albani and Mahowald (2019). The change of global (clearsky) planetary albedo
295 (Figure 1f) indicates that the whole Earth system receives less energy from the Sun and thus
296 should become colder.

297

298 The expansion of sea ice plays an important role in both cooling the climate and weakening the
299 AMOC, but it is unclear why sea ice expands in the first place except that the initial AMOC
300 weakening due to dust removal should have some contribution. This initial (first 25 to 50 years)

301 weakening of AMOC is small (Figure S1b), and is not expected to induce significant sea-ice
302 expansion as can be inferred from the MH results (Zhang et al. 2021). To quantify the
303 contribution of atmospheric and terrestrial components to the global surface cooling after dust
304 removal during LGM, the prescribed-SST experiments are carried out. Result shows that the
305 GMST decreases by 0.31 °C after dust is removed even when SST and sea-ice concentration are
306 fixed (Figure 3a and Table S1). Significant decrease of temperature and increase of albedo occur
307 over some continental regions, especially over high grounds and North Africa and Arabian region
308 (Figures 3a-c), similar to those in the coupled experiments. These changes in temperature and
309 surface albedo over high grounds are due to easier snow accumulation (Figure 3d) after
310 snow-darkening effect is removed. The cooling over land induces global cooling which is
311 amplified over the Arctic region (~ 3 °C; Figure 3a), which cause more significant sea-ice growth
312 than the initial AMOC weakening as will be confirmed by the result of slab-ocean experiments.
313 The result of prescribed-SST experiments also indicates that the ocean and sea-ice dynamics and
314 the feedback between them have a much stronger cooling effect (2.11 °C) during the LGM than
315 during MH.

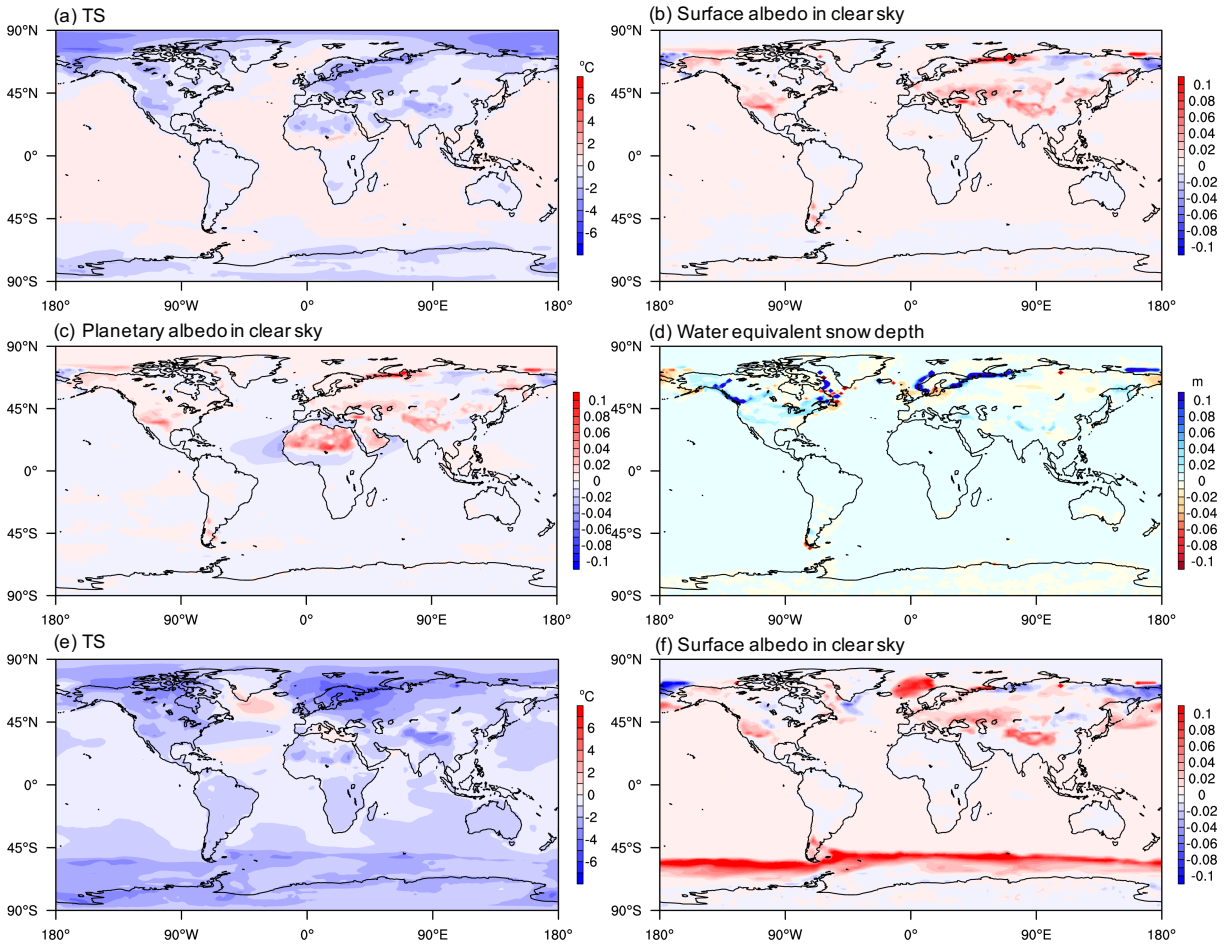
316

317 The result of the slab-ocean experiments shows that a further global surface cooling of 0.90 °C is
318 obtained when sea ice is allowed to grow (Figure 3e and Table S1). Note that this number may
319 not be so accurate since the slab-ocean experiment (with dust) cannot fully reproduce the surface
320 temperature of the coupled experiment, especially over the Southern Ocean (Figure S6).

321 Interestingly, sea ice within the northern North Atlantic decreases when dust is removed (as can
322 be inferred from the surface albedo change in Figure 3f), demonstrating the importance of ocean
323 dynamics to sea-ice growth in this region. These results imply that the weakening of AMOC and

324 the associated feedback from sea-ice expansion lead to an additional cooling of roughly 1.21 °C
 325 (2.42 °C minus 0.31 minus 0.90 °C).

326



327

328 **Figure 3.** Changes of variables when dust is removed in (a-d) prescribed-SST experiments and
 329 (e-f) slab-ocean experiments. All variables are in annual mean, they are: (a) surface temperature
 330 (unit: °C), (b) clear-sky surface albedo, (c) planetary albedo in clear sky, (d) water equivalent
 331 snow depth (unit: m), (e) clear-sky surface temperature (unit: °C) and (f) surface albedo.

332

333 5.2 AMOC change

334 AMOC weakening is due to the surface density reduction over the northern North Atlantic after

335 dust removal, while the density reduction itself is due to salinity reduction since temperature
336 change there tends to increase density (Figure S5). Salinity budget for the top 30 m over
337 deep-water formation region near the Irminger Sea (the green box in Figure 2d, 45° N-65° N, 40°
338 W-10° W) is carried out to understand why salinity decreases there. The variation of salinity is
339 decomposed into four components corresponding to four processes: advection, diffusion, sea ice
340 growth and melting, and net evaporation. More details about how they are calculated could be
341 found in Yang and Wen (2020) and Zhang et al. (2021).

342

343 Result shows that the evolution of salinity near the Irminger Sea can be divided into two stages,
344 at approximately 25th model year. During the first 25 years, the salinity reduction is solely due to
345 horizontal advection while sea-ice melting becomes more and more important afterwards (Figure
346 2d). The vertical advection cannot reduce the surface salinity because the salinity is larger at
347 depth than at the surface in that region (not shown). In the last 200 years, the contributions of
348 sea-ice melting and advection to salinity reduction are comparable (~0.6 psu/year). The two
349 terms are balanced mainly by the diffusion term (Figure 2e), while the net evaporation plays a
350 negligible role.

351

352 During the first stage, the low-salinity water is advected from the lower latitude to the deepwater
353 formation region, similar to what happens in MH (Zhang et al. 2021). The reduction in dust
354 weakens the monsoonal precipitation over North Africa but strengthens the precipitation in the
355 western North Atlantic (Figure 1b), decreasing the sea surface salinity there (Figure S7a). This
356 salinity anomaly is then advected to the high latitudes by the surface ocean currents (Figures
357 S7a-d), causing the weakening of AMOC.

358

359 In the second stage, sea ice in the North Atlantic and Arctic expands and thickens (Figures S7f-h)
360 as a response to the weakening of AMOC and global cooling. This increased sea ice over one of
361 the major deep-water formation regions (green box in Figure 2b) can decrease the surface
362 salinity there directly by melting, as indicated by the blue line in Figure 3. The increased melting
363 of sea ice in the region to the west and south of the deep-water formation region reduces the
364 surface salinity there (Figures S7b-d). This salinity anomaly is also advected to the deep-water
365 formation region by the ocean current, as can be inferred from the concurrent increase of sea-ice
366 and advective contributions to the salinity anomaly since year 25 (Figure 2d). This is the reason
367 why the contribution of advection to salinity anomaly over the deep-water formation region in
368 LGM is significantly greater than that in MH.

369

370 Note that most (~80 %) of the sea ice over the northern North Atlantic is not grown in situ, rather
371 it is transported there from the Arctic ocean (not shown). The melting of such sea ice reduces the
372 surface salinity over the northern North Atlantic (45° N-70° N, up to 2.0 psu; Figure S5b). As a
373 result, the salinity induced density stratification over that region strengthens significantly at the
374 end of the simulation (Figure S5).

375

376 **6. Conclusion and discussion**

377 Opposite to the slight global warming induced by dust removal during MH, a significant cooling
378 of 2.42 °C is obtained for the LGM. However, the AMOC weakens during the LGM when dust is
379 removed, just as in MH, but with a much larger magnitude (-28.7 % vs. -6.2 %). The snow cover
380 and surface albedo increase over high grounds and polar regions due to the removal of

381 snow-darkening effect of the dust. This albedo change induces cooling on land and sea ice, and
382 globally the cooling is 0.31 °C. The thermodynamic sea-ice growth triggered by such cooling
383 induces a further cooling of ~0.90 °C. The rest of the cooling (1.21 °C) is achieved through
384 weakening of AMOC and the positive feedback between sea ice and AMOC. The initial AMOC
385 weakening is due to the advection of negative salinity anomaly to the deep-water formation
386 region from the western North Atlantic. The later weakening is due to increasing sea-ice
387 meltwater within the deep-water formation region both locally and advected from surrounding
388 regions. Our results indicate that the glacial climate and AMOC are much more sensitive to the
389 dust change than their interglacial counterparts; the simulated LGM climate by CESM1.2 would
390 have been much colder if it were not for the existence of dust.

391
392 To test the influence of the uncertainty in dust emission on the results obtained above, we carried
393 out a pair of prescribed-SST experiments with a different dust source distribution. In this
394 distribution, the glaciogenic dust sources (Albani et al. 2014; Mahowald et al. 2006b; Ohgaito et
395 al. 2018) are considered, mainly located in Europe, Siberia, South America and North America
396 (Figure S8a). A total emission of 1090 Tg/year from these additional sources is prescribed
397 according to Albani et al. (2014). Compared to the result in the prescribed-SST LGM experiment
398 described above, the atmospheric dust loading increases near the new dust sources but decreases
399 in Asia, indicating complex interaction between dust and climate (Figure S8c). The total
400 atmospheric dust loading increases slightly by 0.95 Tg and the GMST increases by 0.03 °C
401 (Table S1). This means that removing such dust will induce a cooling of 0.34 °C, only slightly
402 larger than that obtained in section 5.1. The experiments with fully coupled model are therefore
403 not carried out given the expensive computational cost and the likely little gain from the results.

404

405 The GMST of MH is similar to that of PI but with warmer polar regions than PI (Braconnot et al.
406 2007; Brierley et al. 2020; Liu et al. 2018; Zhang et al. 2021). Therefore, the extent of polar sea
407 ice as well as land snow is much smaller than that during the LGM. The removal of dust does not
408 induce significant cooling over land or sea ice, making the surface albedo feedback of sea ice
409 and land snow as well as the interaction between AMOC and sea ice negligible. The result is
410 subject to uncertainties since it is obtained with only a single model. Most other models may
411 obtain smaller climatic impact of dust since their LGM climates are warmer and snow and
412 sea-ice are less than those obtained by CESM1.2.2 (Kageyama et al. 2021).

413

414 **Acknowledgments**

415 This work is supported by Chinese MOST 2017YFA0603801, NSFC 41888101 and NSFC
416 41630527. We greatly appreciate the invaluable suggestions from Prof. Samuel Albani at
417 University of Milano-Bicocca and Prof. Zhengguo Shi at Institute of Earth Environment,
418 Chinese Academy of Sciences. Simulations were performed on the Thanhe-2 Supercomputer at
419 the Chinese National Supercomputer Center in Guangzhou and the High-performance
420 Computing Platform of Peking University. The authors declare that they have no competing
421 interests.

422

423 **Data Availability Statement**

424 Relevant datasets generated in this study are available on Zenodo with the identifier
425 <https://zenodo.org/record/5576923#.YW4vNLhByUk>.

426

427 **References**

- 428 Adkins, J. F., K. McIntyre, and D. P. Schrag, 2002: The salinity, temperature, and delta O-18 of
429 the glacial deep ocean. *Science*, **298**, 1769-1773.
- 430 Adkins, J. F., A. P. Ingersoll, and C. Pasquero, 2005: Rapid climate change and conditional
431 instability of the glacial deep ocean from the thermobaric effect and geothermal heating.
432 *Quaternary Sci Rev*, **24**, 581-594.
- 433 Albani, S., and N. M. Mahowald, 2019: Paleodust Insights into Dust Impacts on Climate. *J*
434 *Climate*, **32**, 7897-7913.
- 435 Albani, S., and Coauthors, 2014: Improved dust representation in the Community Atmosphere
436 Model. *J Adv Model Earth Sy*, **6**, 541-570.
- 437 Bohm, E., and Coauthors, 2015: Strong and deep Atlantic meridional overturning circulation
438 during the last glacial cycle. *Nature*, **517**, 73-U170.
- 439 Braconnot, P., and Coauthors, 2007: Results of PMIP2 coupled simulations of the Mid-Holocene
440 and Last Glacial Maximum - Part 1: experiments and large-scale features. *Clim Past*, **3**, 261-277.
- 441 Briegleb, B. P., G. Danabasoglu, and W. G. Large, 2010: An overflow parameterization for the
442 ocean component of the Community Climate System Model. *NCAR Tech*, **Note NCAR/**
443 **TN-4811STR, 72 pp.**
- 444 Brierley, C. M., and Coauthors, 2020: Large-scale features and evaluation of the PMIP4-CMIP6
445 midHolocene simulations. *Clim Past*, **16**, 1847-1872.
- 446 Brovkin, V., A. Ganopolski, D. Archer, and S. Rahmstorf, 2007: Lowering of glacial atmospheric
447 CO₂ in response to changes in oceanic circulation and marine biogeochemistry.
448 *Paleoceanography*, **22**.
- 449 Curry, W. B., and D. W. Oppo, 2005: Glacial water mass geometry and the distribution of delta

450 C-13 of Sigma CO₂ in the western Atlantic Ocean. *Paleoceanography*, **20**.

451 Danabasoglu, G., and Coauthors, 2012: The CCSM4 Ocean Component. *J Climate*, **25**,
452 1361-1389.

453 deMenocal, P., J. Ortiz, T. Guilderson, J. Adkins, M. Sarnthein, L. Baker, and M. Yarusinsky,
454 2000: Abrupt onset and termination of the African Humid Period: rapid climate responses to
455 gradual insolation forcing. *Quaternary Sci Rev*, **19**, 347-361.

456 Denton, G. H., R. F. Anderson, J. R. Toggweiler, R. L. Edwards, J. M. Schaefer, and A. E.
457 Putnam, 2010: The Last Glacial Termination. *Science*, **328**, 1652-1656.

458 Flanner, M. G., and C. S. Zender, 2006: Linking snowpack microphysics and albedo evolution. *J*
459 *Geophys Res-Atmos*, **111**.

460 Flanner, M. G., C. S. Zender, P. G. Hess, N. M. Mahowald, T. H. Painter, V. Ramanathan, and P.
461 J. Rasch, 2009: Springtime warming and reduced snow cover from carbonaceous particles.
462 *Atmos Chem Phys*, **9**, 2481-2497.

463 Ganopolski, A., R. Calov, and M. Claussen, 2010: Simulation of the last glacial cycle with a
464 coupled climate ice-sheet model of intermediate complexity. *Clim Past*, **6**, 229-244.

465 Hansen, J., and L. Nazarenko, 2004: Soot climate forcing via snow and ice albedos. *P Natl Acad*
466 *Sci USA*, **101**, 423-428.

467 Hansson, M. E., 1994: The Renland Ice Core - a Northern-Hemisphere Record of Aerosol
468 Composition over 120,000 Years. *Tellus B*, **46**, 390-418.

469 Harrison, S. P., K. E. Kohfeld, C. Roelandt, and T. Claquin, 2001: The role of dust in climate
470 changes today, at the last glacial maximum and in the future. *Earth-Sci Rev*, **54**, 43-80.

471 Huo, Y., W. R. Peltier, and D. Chandan, 2021: Mid-Holocene monsoons in South and Southeast
472 Asia: dynamically downscaled simulations and the influence of the Green Sahara.

- 473 Kageyama, M., and Coauthors, 2021: The PMIP4 Last Glacial Maximum experiments:
474 preliminary results and comparison with the PMIP3 simulations. *Clim Past*, **17**, 1065-1089.
- 475 Kageyama, M., and Coauthors, 2017: The PMIP4 contribution to CMIP6-Part 4: Scientific
476 objectives and experimental design of the PMIP4-CMIP6 Last Glacial Maximum experiments
477 and PMIP4 sensitivity experiments. *Geosci Model Dev*, **10**, 4035-4055.
- 478 Knutti, R., D. Masson, and A. Gettelman, 2013: Climate model genealogy: Generation CMIP5
479 and how we got there. *Geophys Res Lett*, **40**, 1194-1199.
- 480 Kohfeld, K. E., and S. P. Harrison, 2001: DIRTMAP: the geological record of dust. *Earth-Sci*
481 *Rev*, **54**, 81-114.
- 482 Lambert, F., and Coauthors, 2008: Dust-climate couplings over the past 800,000 years from the
483 EPICA Dome C ice core. *Nature*, **452**, 616-619.
- 484 Lawrence, D. M., and Coauthors, 2011: Parameterization Improvements and Functional and
485 Structural Advances in Version 4 of the Community Land Model. *J Adv Model Earth Sy*, **3**.
- 486 Liu, Y. G., M. Zhang, Z. Y. Liu, Y. Xia, Y. Huang, Y. R. Peng, and J. Zhu, 2018: A Possible Role
487 of Dust in Resolving the Holocene Temperature Conundrum. *Sci Rep-Uk*, **8**.
- 488 Lynch-Stieglitz, J., and Coauthors, 2007: Atlantic meridional overturning circulation during the
489 Last Glacial Maximum. *Science*, **316**, 66-69.
- 490 Maher, B. A., J. M. Prospero, D. Mackie, D. Gaiero, P. P. Hesse, and Y. Balkanski, 2010: Global
491 connections between aeolian dust, climate and ocean biogeochemistry at the present day and at
492 the last glacial maximum. *Earth-Sci Rev*, **99**, 61-97.
- 493 Mahowald, N. M., M. Yoshioka, W. D. Collins, A. J. Conley, D. W. Fillmore, and D. B. Coleman,
494 2006a: Climate response and radiative forcing from mineral aerosols during the last glacial
495 maximum, pre-industrial, current and doubled-carbon dioxide climates. *Geophys Res Lett*, **33**.

496 Mahowald, N. M., D. R. Muhs, S. Levis, P. J. Rasch, M. Yoshioka, C. S. Zender, and C. Luo,
497 2006b: Change in atmospheric mineral aerosols in response to climate: Last glacial period,
498 preindustrial, modern, and doubled carbon dioxide climates. *J Geophys Res-Atmos*, **111**.

499 Marchitto, T. M., and W. S. Broecker, 2006: Deep water mass geometry in the glacial Atlantic
500 Ocean: A review of constraints from the paleonutrient proxy Cd/Ca. *Geochem Geophys Geosy*, **7**.

501 Mashayek, A., and W. R. Peltier, 2013: Shear-induced mixing in geophysical flows: does the
502 route to turbulence matter to its efficiency? *J Fluid Mech*, **725**, 216-261.

503 Mayewski, P. A., and Coauthors, 1994: Changes in Atmospheric Circulation and Ocean Ice
504 Cover over the North-Atlantic during the Last 41,000 Years. *Science*, **263**, 1747-1751.

505 McGee, D., P. B. deMenocal, G. Winckler, J. B. W. Stuut, and L. I. Bradtmiller, 2013: The
506 magnitude, timing and abruptness of changes in North African dust deposition over the last
507 20,000 yr. *Earth Planet Sc Lett*, **371**, 163-176.

508 Neale, R. B., and Coauthors, 2010: Description of the NCAR Community Atmosphere Model
509 (CAM 5.0).

510 Ohgaito, R., and Coauthors, 2018: Effect of high dust amount on surface temperature during the
511 Last Glacial Maximum: a modelling study using MIROC-ESM. *Clim Past*, **14**, 1565-1581.

512 Pausata, F. S. R., G. Messori, and Q. Zhang, 2016: Impacts of dust reduction on the northward
513 expansion of the African monsoon during the Green Sahara period. *Earth Planet Sc Lett*, **434**,
514 298-307.

515 Pausata, F. S. R., and Coauthors, 2017a: Tropical cyclone activity enhanced by Sahara greening
516 and reduced dust emissions during the African Humid Period. *P Natl Acad Sci USA*, **114**,
517 6221-6226.

518 Pausata, F. S. R., and Coauthors, 2017b: Greening of the Sahara suppressed ENSO activity

519 during the mid-Holocene. *Nature Communications*, **8**.

520 Peltier, W. R., D. F. Argus, and R. Drummond, 2015: Space geodesy constrains ice age terminal
521 deglaciation: The global ICE-6G_C (VM5a) model. *J Geophys Res-Sol Ea*, **120**, 450-487.

522 Petit, J. R., L. Mounier, J. Jouzel, Y. S. Korotkevich, V. I. Kotlyakov, and C. Lorius, 1990:
523 Palaeoclimatological and Chronological Implications of the Vostok Core Dust Record. *Nature*,
524 **343**, 56-58.

525 Qian, Y., and Coauthors, 2014: Light-absorbing particles in snow and ice: Measurement and
526 modeling of climatic and hydrological impact. *Adv Atmos Sci*, **32**, 64-91.

527 Sagoo, N., and T. Storelvmo, 2017: Testing the sensitivity of past climates to the indirect effects
528 of dust. *Geophys Res Lett*, **44**, 5807-5817.

529 Shen, J. J., X. N. Xie, X. G. Cheng, and X. D. Liu, 2020: Effects of dust-in-snow forcing over
530 the Tibetan Plateau on the East Asian dust cycle during the Last Glacial Maximum. *Palaeogeogr*
531 *Palaeocl*, **542**.

532 Shi, Z. G., and Coauthors, 2019: Snow-darkening versus direct radiative effects of mineral dust
533 aerosol on the Indian summer monsoon onset: role of temperature change over dust sources.
534 *Atmos Chem Phys*, **19**, 1605-1622.

535 Smith, R. D., and P. Gent, 2010: The Parallel Ocean Program (POP) reference manual, ocean
536 component of the Community Climate System Model (CCSM). *Los Alamos National Laboratory*
537 *Tech. Rep*, **LAUR-10-01853**, 141 pp

538 Steffensen, J. P., 1997: The size distribution of microparticles from selected segments of the
539 Greenland Ice Core Project ice core representing different climatic periods. *J Geophys*
540 *Res-Oceans*, **102**, 26755-26763.

541 Steffensen, J. P., and Coauthors, 2008: High-resolution Greenland Ice Core data show abrupt

542 climate change happens in few years. *Science*, **321**, 680-684.

543 Sun, W. Y., and Coauthors, 2019: Northern Hemisphere Land Monsoon Precipitation Increased
544 by the Green Sahara During Middle Holocene. *Geophys Res Lett*, **46**, 9870-9879.

545 Takemura, T., M. Egashira, K. Matsuzawa, H. Ichijo, R. O'ishi, and A. Abe-Ouchi, 2009: A
546 simulation of the global distribution and radiative forcing of soil dust aerosols at the Last Glacial
547 Maximum. *Atmos Chem Phys*, **9**, 3061-3073.

548 Thompson, A. J., C. B. Skinner, C. J. Poulsen, and J. Zhu, 2019: Modulation of Mid-Holocene
549 African Rainfall by Dust Aerosol Direct and Indirect Effects. *Geophys Res Lett*, **46**, 3917-3926.

550 Tierney, J. E., J. Zhu, J. King, S. B. Malevich, G. J. Hakim, and C. J. Poulsen, 2020: Glacial
551 cooling and climate sensitivity revisited. *Nature*, **584**, 569-+.

552 Werner, M., and Coauthors, 2002: Seasonal and interannual variability of the mineral dust cycle
553 under present and glacial climate conditions. *J Geophys Res-Atmos*, **107**.

554 Yang, H. J., and Q. Wen, 2020: Investigating the Role of the Tibetan Plateau in the Formation of
555 Atlantic Meridional Overturning Circulation. *J Climate*, **33**, 3585-3601.

556 Zhang, M., Y. Liu, J. Zhang, and Q. Wen, 2021: AMOC and Climate Responses to Dust
557 Reduction and Greening of the Sahara during the Mid-Holocene. *J Climate*, **34**, 4893-4912.

558 Zheng, W., B. Wu, J. He, and Y. Yu, 2013: The East Asian Summer Monsoon at mid-Holocene:
559 results from PMIP3 simulations. *Clim Past*, **9**, 453-466.

560 Zhu, J., and C. J. Poulsen, 2021: Last Glacial Maximum (LGM) climate forcing and ocean
561 dynamical feedback and their implications for estimating climate sensitivity. *Clim Past*, **17**,
562 253-267.

563

564

1
2
3
4
5
6
7
8
9
10
11
12
13
14
15
16
17
18
19
20

Geophysical Research Letters

Supporting Information for

**Impact of Dust on climate and AMOC during the Last Glacial Maximum Simulated
by CESM1.2**

Ming Zhang¹, Yonggang Liu^{1*}, Jiang Zhu², Zhuoqun Wang¹, Zhengyu Liu³

¹ Laboratory for Climate and Ocean-Atmosphere Studies, Department of Atmospheric and
Oceanic Sciences, School of Physics, Peking University, Beijing, 100871, China

² Climate and Global Dynamics Laboratory, National Center for Atmospheric Research,
Boulder, CO, 80305, USA

³ Atmospheric Science Program, Department of Geography, Ohio State University, Columbus,
Ohio, 43210, USA.

Contents of this file

Text S1

Figures S1 to S8

Table S1

21 **Text S1.** Supporting information for the experimental setup.

22

23 To understand the mechanisms of climate change more clearly, we carried out a pair of
24 atmosphere-only experiments, one with dust (called LGM_fixedSST) and the other without
25 (called LGMND_fixedSST), in which the sea surface temperature (SST) and sea-ice
26 concentration from the fully coupled experiment LGMctl are prescribed. The climate
27 forcings (e.g., orbital parameters, GHGs, LISs, vegetation and dust) in both experiments are
28 the same as those in the coupled experiments (i.e., LGMctl and LGMND). Both experiments
29 were run for 20 years and the final 5 years of data are used for analysis. The simulated GMST
30 and global dust loading in the control experiment are 7.56 °C and 41.79 Tg, respectively,
31 close to the numbers in the fully coupled experiment (LGMctl) (Table S1).

32

33 In order to quantify the contribution of ocean dynamics to surface temperature change, we
34 performed a pair of slab-ocean experiments without ocean dynamics (called LGM_SOM and
35 LGMND_SOM). The slab ocean model (SOM) uses prescribed heat transport convergence (q
36 flux) and mixed layer depth derived from LGMctl. Settings for the orbital parameters, GHGs,
37 LISs, vegetation and dust in both experiments are the same as those in LGMctl and LGMND.
38 Both of the with-dust and without-dust experiments were run for 40 years and the final 10
39 years of data are used for analysis. The GMST in the slab-ocean experiment with dust is
40 8.82 °C, ~1 °C higher than that in LGMctl. The most significant warming occurs over the
41 high latitudes of Southern Hemisphere (Figure S6). This difference in surface temperature

42 may have some influence on the estimated impact of sea-ice expansion on temperature, but is
43 likely small (related discussion can be found in section 5.1 of the main text). The simulated
44 global dust loading is 42.62 Tg, similar to that in the fully coupled experiment (LGMctl).

45

46 To test the influence of the uncertainty in dust emission, we carried out a pair of
47 prescribed-SST experiments with a different dust source distribution. One of them is the same
48 as the prescribed-SST experiment with dust described above. In the other (called
49 LGM_fixedSST_gladst), the glaciogenic emission of 1090 Tg/year in total from Albani et al.
50 (2014) is considered in addition (Figure S8a, b). The glaciogenic dust flux is prescribed in the
51 model, mainly located in Europe, Siberia, South America and North America (Figure S8a).

52 The experiments were run for 20 years and the final 5 years of data are used for analysis.

53

54

55

56

57

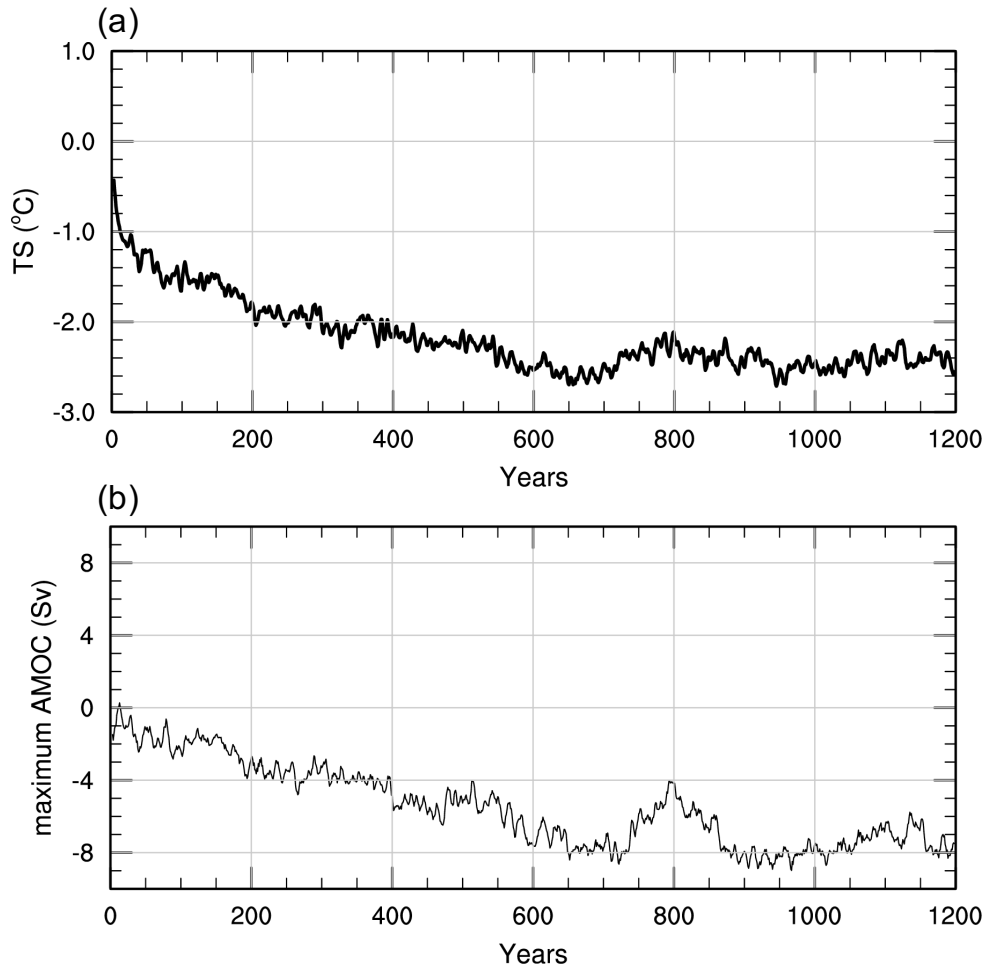
58

59

60

61

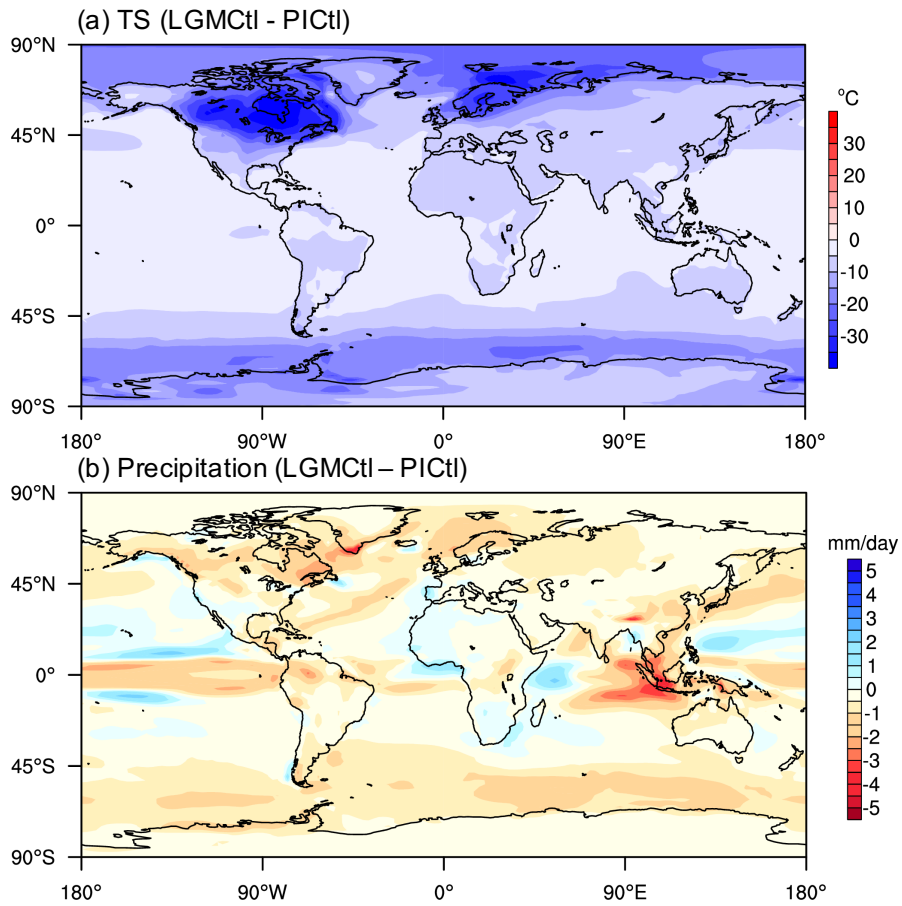
62



63

64 **Figure S1.** Evolution of anomalies of (a) global annual-mean surface temperature (unit: °C)
65 and (b) maximum AMOC below 500 m depth (unit: Sv) in the LGMND experiment relative
66 to the control simulation LGMCtl. A 5-yr running mean filter has been applied to both curves.

67



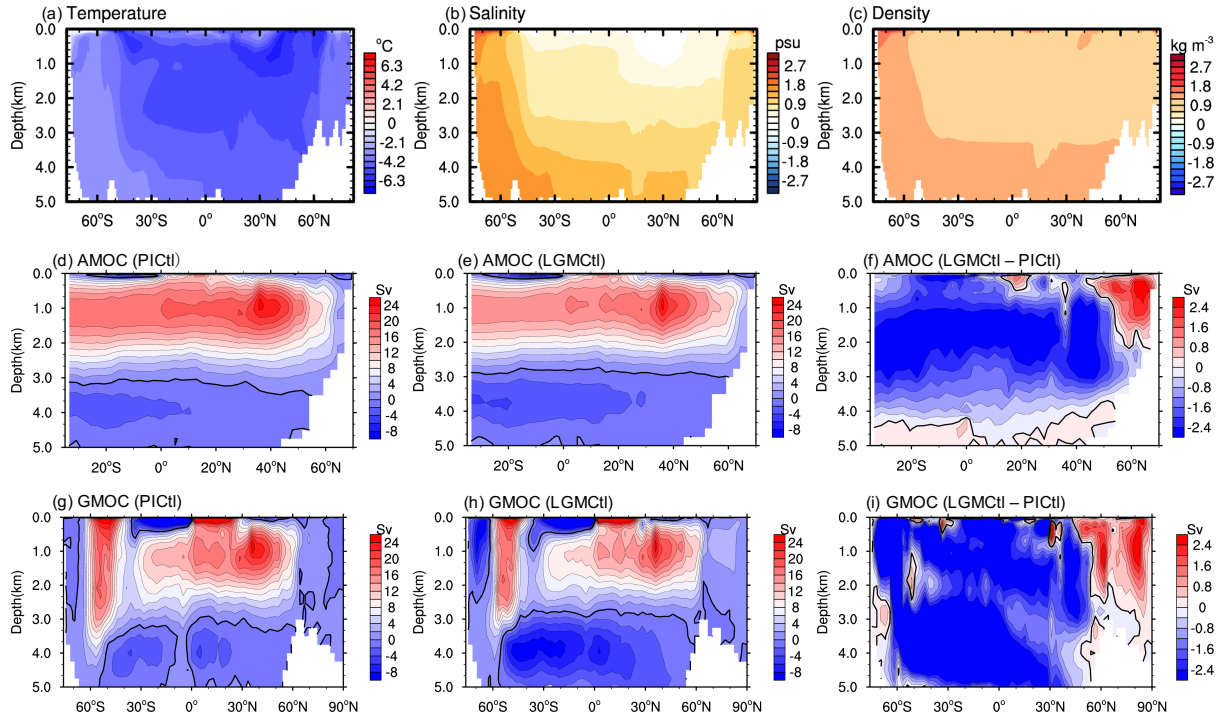
68

69 **Figure S2.** Simulated annual mean (a) surface temperature anomaly (unit: °C) and (b)

70 precipitation (unit: mm/day) in the LGMctl experiment compared to PI.

71

72



73

74 **Figure S3.** Anomalies of zonal mean (a) potential temperature (unit: °C), (b) salinity (unit:

75 psu) and (c) potential density (unit: kg m^{-3}) in the Atlantic Ocean for experiment LGMcI

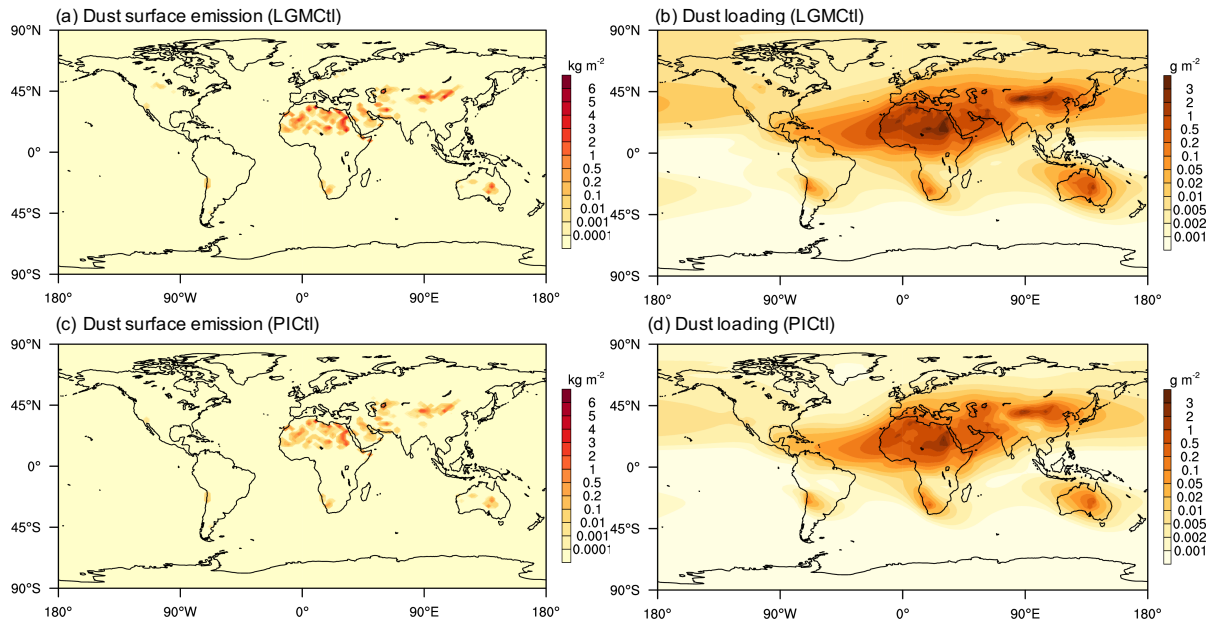
76 relative to PI. Annual mean Atlantic meridional streamfunction (AMSF, unit: Sv) for PI and

77 LGM is shown in (d) and (e), respectively. The AMSF difference between LGM and PI is

78 shown in (f). Figures g-i are similar to d-f but for the global meridional streamfunction

79 (GMSF, unit: Sv). The zero contour lines are shown in black.

80



81

82 **Figure S4.** Annual mean dust emission (unit: kg m^{-2}) and dust loading (unit: g m^{-2}) for LGM

83 (a-b) and PI (c-d).

84

85

86

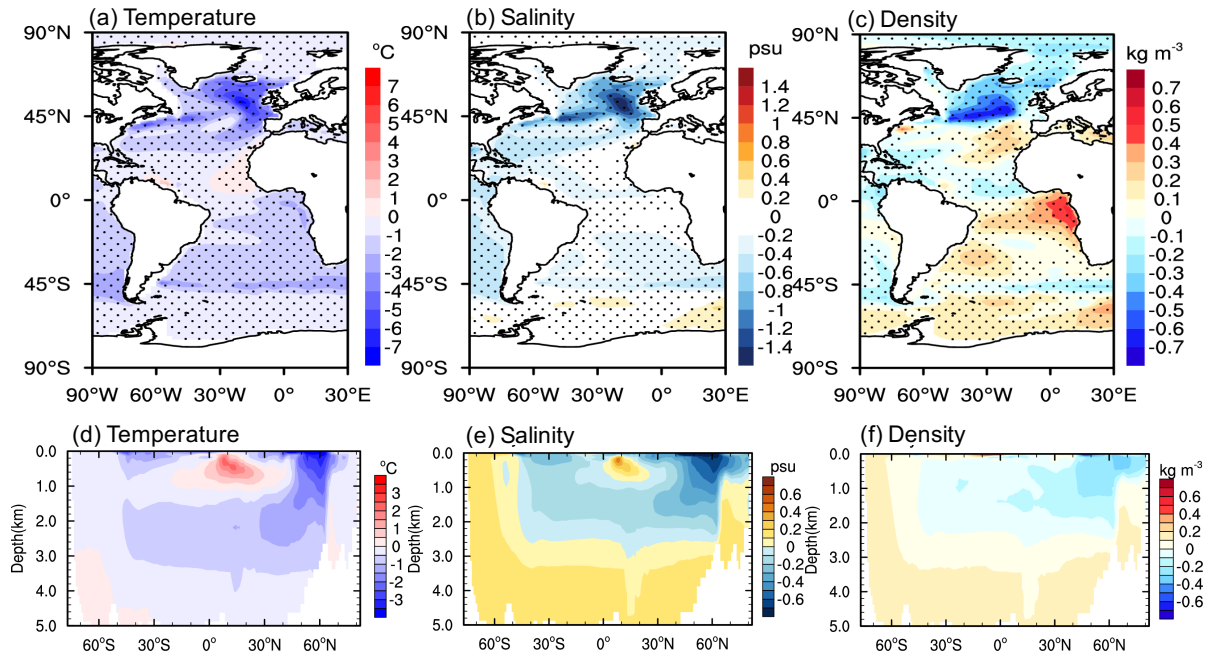
87

88

89

90

91



92

93

Figure S5. Anomalies of annual mean surface (top 100 m) (a) potential temperature

94

(unit: °C), (b) salinity (unit: psu) and (c) potential density (unit: kg m^{-3}) over the Atlantic

95

Ocean for the LGMND experiment compared to LGMctl and anomalies of zonal mean (d)

96

potential temperature, (e) salinity and (f) potential density in the Atlantic Ocean for LGMND

97

compared to LGMctl.

98

99

100

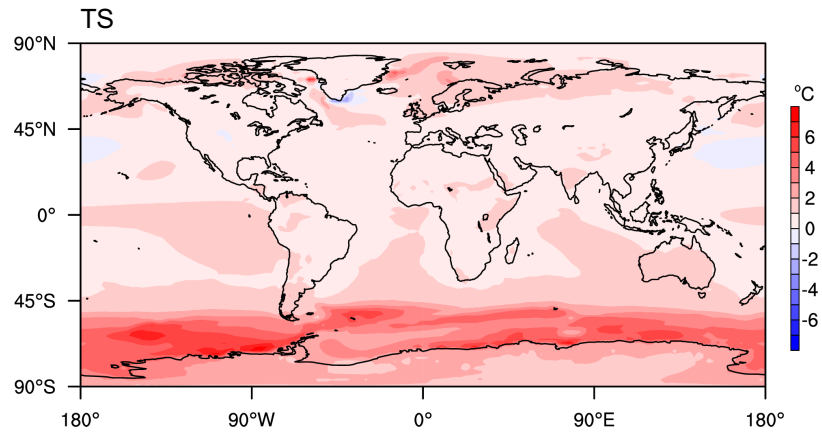
101

102

103

104

105



106

107 **Figure S6.** Difference of annual mean surface temperature (unit: °C) between the LGM

108 control experiments with slab ocean model and fully coupled model.

109

110

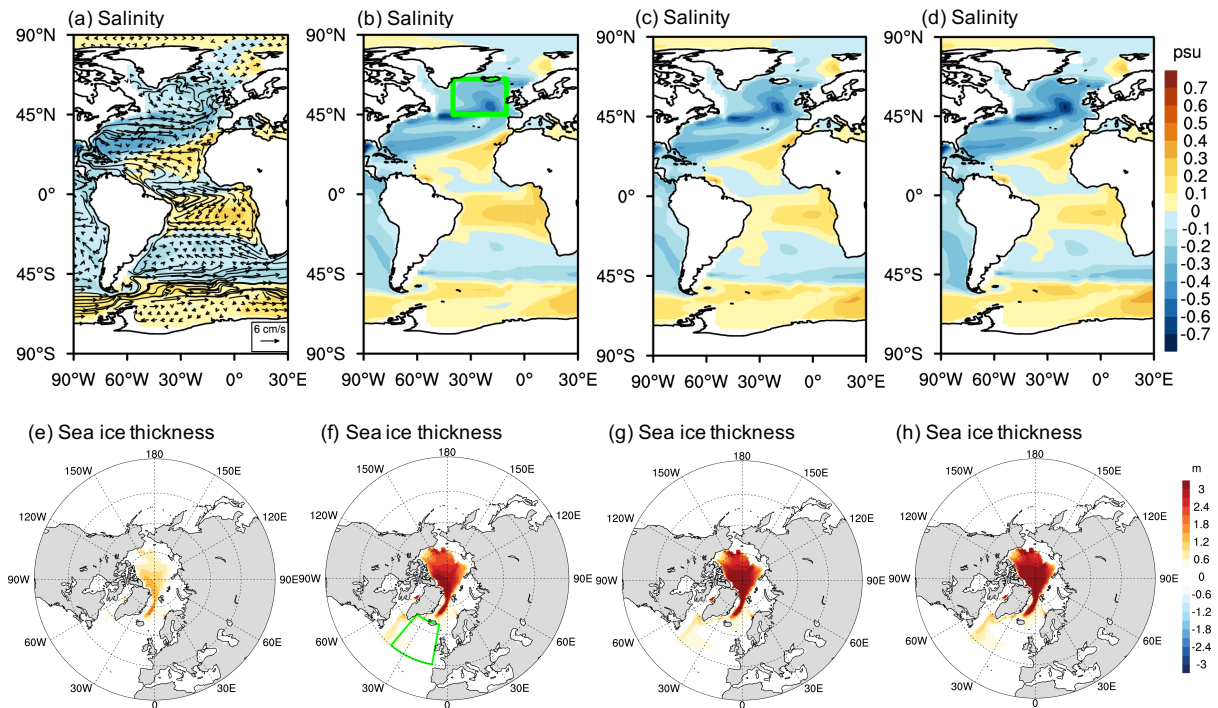
111

112

113

114

115



116

117 **Figure S7.** Changes of annual mean sea surface (top 100 m) salinity (unit: psu) in Atlantic

118 (upper row) and annual mean sea-ice thickness (unit: m) in Arctic (bottom row) averaged

119 over (a), (b) year 1-50; (c), (d) year 51-100; (e), (f) year 101-150; (g), (h) year 151-200 after

120 dust removal. Vectors in (a) show the annual-mean surface (top 100 m) ocean current in

121 LGMctl (unit: cm/s). The green boxes (45° N- 65° N, 40° W- 10° W) in (b) and (f) show

122 where salinity budget is calculated.

123

124

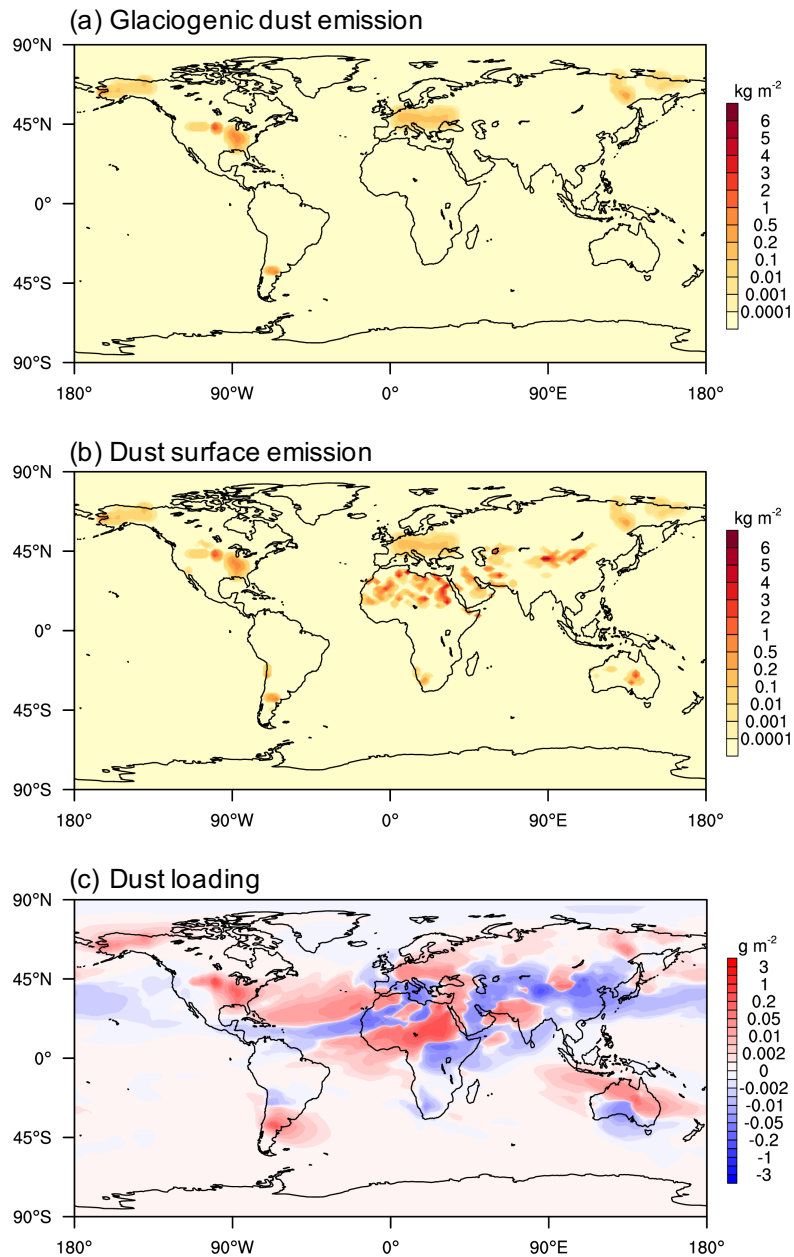
125

126

127

128

129



131

132 **Figure S8.** (a) Glaciogenic dust flux (unit: kg m^{-2}) from Albani et al. (2014), (b) total dust133 emissions (including glaciogenic and non-glaciogenic dust emissions) (unit: kg m^{-2}) in our134 simulation, (c) difference of annual-mean dust loading (unit: g m^{-2}) between the experiments

135 with additional glaciogenic dust and without glaciogenic dust.

136

137

138

139 **Table S1.** Summary of the experiment parameters and results. TS and Prec. are the global annual-mean surface temperature and precipitation,
 140 respectively. Max. AMOC is defined as the maximum Atlantic meridional streamfunction below 500 m depth.

Experiment	LGM control (LGMctl)	No dust (LGMND)	LGM_fixedSST	LGMND_fixedSST	LGM_SOM	LGMND_SOM	LGM_fixedSST_gladst
Orbit	21 ka	21 ka	21 ka	21 ka	21 ka	21 ka	21 ka
CO ₂ (ppm)	185	185	185	185	185	185	185
CH ₄ (ppb)	350	350	350	350	350	350	350
N ₂ O (ppb)	200	200	200	200	200	200	200
Ice sheets	ICE-6G	ICE-6G	ICE-6G	ICE-6G	ICE-6G	ICE-6G	ICE-6G
Topography Coastlines	ICE-6G	ICE-6G	ICE-6G	ICE-6G	ICE-6G	ICE-6G	ICE-6G
Duration (year)	4000	1200	20	20	40	40	20
TS (°C)	7.66	5.24	7.57	7.26	8.82	7.61	7.60
Prec. (mm/day)	2.57	2.52	2.55	2.66	2.64	2.67	2.56
Max. AMOC (Sv)	24.79	17.08	-	-	-	-	-
TS trend (°C/kyr)	0.056	-0.15	-	-	-	-	-
AMOC trend (Sv/kyr)	-0.18	-2.16	-	-	-	-	-
Dust emissions (Tg)	6369.17	0	6329.89	0	6314.89	0	7472.02
Dust loading (Tg)	41.96	0	41.79	0	42.62	0	42.74

141

142